# Spatial measurement in rotating magnetic field plasma acceleration method by using two-dimensional scanning instrument and thrust stand

T. Furukawa, K. Takizawa, K. Yano, D. Kuwahara, and S. Shinohara

Citation: Review of Scientific Instruments **89**, 043505 (2018); doi: 10.1063/1.5013214
View online: https://doi.org/10.1063/1.5013214
View Table of Contents: http://aip.scitation.org/toc/rsi/89/4
Published by the American Institute of Physics

# Spatial measurement in rotating magnetic field plasma acceleration method by using two-dimensional scanning instrument and thrust stand

T. Furukawa,[1,a)] K. Takizawa,[1] K. Yano,[1] D. Kuwahara,[2] and S. Shinohara[2]
[1]*The Graduate School of Engineering, Tokyo University of Agriculture and Technology, Tokyo 184-8588, Japan*
[2]*Institute of Engineering, Tokyo University of Agriculture and Technology, Tokyo 184-8588, Japan*

(Received 11 November 2017; accepted 18 March 2018; published online 6 April 2018)

A two-dimensional scanning probe instrument has been developed to survey spatial plasma characteristics in our electrodeless plasma acceleration schemes. In particular, diagnostics of plasma parameters, e.g., plasma density, temperature, velocity, and excited magnetic field, are essential for elucidating physical phenomena since we have been concentrating on next generation plasma propulsion methods, e.g., Rotating Magnetic Field plasma acceleration method, by characterizing the plasma performance. Moreover, in order to estimate the thrust performance in our experimental scheme, we have also mounted a thrust stand, which has a target type, on this movable instrument, and scanned the axial profile of the thrust performance in the presence of the external magnetic field generated by using permanent magnets, so as to investigate the plasma captured in a stand area, considering the divergent field lines in the downstream region of a generation antenna. In this paper, we will introduce the novel measurement instrument and describe how to measure these parameters. *Published by AIP Publishing.*
https://doi.org/10.1063/1.5013214

## I. INTRODUCTION

Plasma diagnostics[1] are widely conducted to investigate the physical phenomena of plasma and estimate an influence of plasma existence. For instance, in the field of a recent plasma industry, plasma processing technology has been developed rapidly, causing the advancement of a semiconductor production due to today's enormous social needs with respect to information technology, electronic devices, and tools. Among such a trend, characterizing plasma parameters is crucial since more detailed understanding of plasma behaviors is required. In particular, spatial profiles of plasma parameters, e.g., plasma density, temperature, and drift velocity, as well as ac and dc magnetic fields for understanding variable electrostatic and electromagnetic instabilities excited in plasmas,[2] are interesting in terms of spatial uniformity for the reproducibility and accuracy in making much smaller precision device, e.g., Large Scale Integration (LSI).

Similarly, in the field of plasma propulsion scheme, a spatial profile measurement of important plasma parameters is being carried out to estimate the acceleration effect and the thrust performance. As *in situ* plasma diagnostics, some measurement techniques have been adopted: Langmuir probe,[3] Mach probe,[4,5] and double probe[6] are major methods due to an easy introduction of local values, although these tools may disturb plasma flow and affect the plasma characteristics. On the contrary, electromagnetic and spectroscopy methods, e.g., microwave interferometer,[7] Laser Induced Fluorescence (LIF) method,[8–10] and Laser Thomson Scattering (LTS),[11] are effective ways in terms of non-direct contact measurements with a plasma with good measurement accuracy. In the field of nuclear fusion plasma research, these measurement methods are also utilized widely, reducing contaminations by impurities under the extremely high temperature conditions. However, these measurement devices are typically expensive and generally complicated.

As a measurement tool in our experimental plasma acceleration scheme, a two-dimensional scanning instrument inserted into a plasma has been developed. Various kinds of probes, as described above, can be attached on this instrument and the moving step size and its direction are controlled by using stepping motors and a Peripheral Interface Controller (PIC, Microchip Technology, Inc.) micro-controller system. This device is useful for spatial measurements to monitor various plasma parameters. Here, the developed scanning instrument has the lower height of a rail board, where movable mechanisms can move axially, considering the device geometry and disturbance of plasma flow. An electron density $n_e$ and an ion velocity $v_i$ have been measured to elucidate plasma performance by our electrodeless acceleration schemes, proposed under a Helicon Electrodeless Advanced Thruster (HEAT) project,[12,13] e.g., Rotating Magnetic Field (RMF)[14,15] acceleration[16–18] method.[12,13,19]

Here, brief explanation of our plasma acceleration scheme will be described as follows, regarding the RMF acceleration scheme. Recently, helicon electrodeless plasma acceleration systems have been studied for next generation plasma thrusters. In this scheme, helicon wave[20] is expected to be excited by using an external antenna and high-dense plasma, up to $\sim 10^{13}$ cm$^{-3}$, can be obtained with broad operation conditions. This production scheme has no direct-interaction between electrodes and plasma, reducing wear of electrodes, and therefore longer operating time can be achieved than that of conventional electric plasma thrusters, including additional acceleration schemes, e.g., ion gridded engine,[21] Hall thruster,[22] and Magneto-Plasma-Dynamics (MPD) thruster,[23]

a)Electronic mail: s172832r@st.go.tuat.ac.jp

and this advantage enables us to probe space phenomena further away. Previously, we have investigated plasma parameters as well as these dependencies on external operation parameters, e.g., radio frequency (rf) power applied to generation antenna, gas flow rate *fr*, in addition to RMF operation conditions.[17,18] Originally, the RMF method was utilized to induce an azimuthal current $j_\theta$ to maintain a Field Reversed Configuration (FRC) in magnetically confined plasma fusion research.[13] We have tried applying this method to an electric thruster under the open magnetic field as the electrodeless plasma acceleration method, with an expectation to generate the axial Lorentz force derived from the cross product of the induced current by the RMF and radial component of the external field. In this paper, we will also show experimental results of the RMF acceleration method using the developed measurement instruments.

As a spatial measurement in using the RMF method, a time-varying perpendicular, one-directional (1D) component of RMF relevant to axial and radial motions has been measured to demonstrate the field penetration into plasma spatially that will be explained later. In addition, a target type thrust stand, which can be mounted on the movable instrument, has been developed, and thrust performance has been measured, using two permanent magnet arrays.[24] Comparison of plasma thrust between the stand measurement and that integrated from plasma parameters by using an electrostatic probe, which showed good agreement with each other w/RMF condition, was made. Here, this probe measurement was conducted at the same time of the thrust measurement. Furthermore, the axial profile of plasma thrust has also been measured, considering the shape of external magnetic field lines by the magnet arrays, and the validity of the measurement was clarified.

The contents in this paper are as follows: Experimental setup of the two-dimensional scanning instrument is described in Sec. II, including present experimental devices and some diagnostics to estimate the plasma performance along with the validity of the developed thrust stand. Spatial measurement results by using the developed instrument, including 1D, rf RMF spatial profiles and thrust performance are shown in Sec. III. Here, present RMF experiments have been conducted in cases of RMF current frequency $f_{\mathrm{RMF}}$ of 0.7 MHz with the acceleration phase $\phi$ of 90° between two sets of antenna current.[17] Finally, conclusion including spatial estimation of the RMF penetration condition into plasma and thrust increment is described in Sec. IV.

## II. EXPERIMENTAL SETUP

### A. Plasma generation and acceleration devices

Figure 1 shows the diagram of a Large Mirror Device (LMD),[25] and it has a 1700 mm-long and 445 mm-diameter vacuum chamber which is connected to a tapered quartz tube of 1000 mm long and 100–170 mm inner diameter, reducing an collision interaction between a plasma and the inner wall in the presence of the divergent magnetic field. This device has two Turbo-Molecular Pumps (TMP), whose pumping speeds are 1000 and 2400 l/s with a base pressure of a few $10^{-4}$ Pa. As a propellant, Ar gas is injected through a head flange port at $z = -1000$ mm. At the stage of rf plasma generation, a half-helical type antenna, whose azimuthal mode is $m = 1$,[26] made of oxygen free copper, is wound around the quartz tube in the permanent magnet region. Generated plasma is expected to be accelerated by using an RMF antenna, whose details including the acceleration mechanism and how to generate the azimuthal current $j_\theta$ are described in Refs. 14, 17, and 18. Detailed description of the scanning instrument in the vacuum chamber is given in Sec. II B.

### B. Design and fabrication of two-dimensional scanning instrument

A two-dimensional scanning instrument has been developed, as shown in Fig. 2. This instrument is composed of an aluminum rail board and axial and radial moving units, and these two-directional movements (every 1 mm) are done by using each stepping motor, controlled by using a PIC micro-controller, and the spatial resolution is good enough to derive the spatial gradient concerning in plasma acceleration. The height of the rail board is low enough not to disturb the plasma flow. The axial and radial moving units can be moved by the use of rack gears and stepping motors with a pinion gear. Wirings connecting the motors and a controller are bundled and covered by using a glass sleeve to prevent the plasma contact. Here, we can install various kinds of probes on the radial moving unit by using two holding units, and a Mach probe and a magnetic probe were used to investigate the plasma parameters and time-varying component of RMF, respectively. Radially centered position of these probe tips is adjusted by using a collimated laser injection at $r = 0$ mm from head/back flange windows of LMD. The two-dimensional experimental results of 1D, rf RMF component are shown in Sec. III.

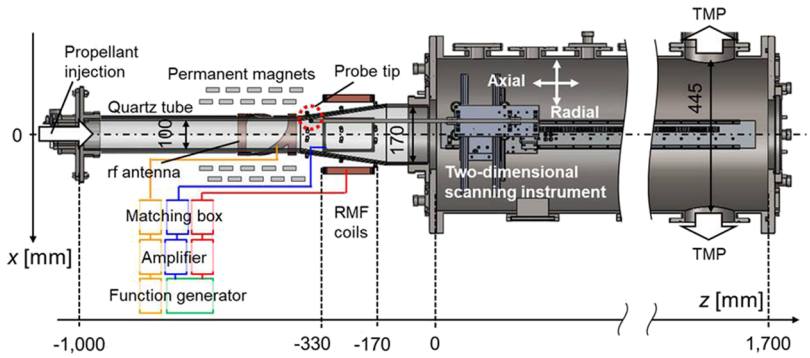


FIG. 1. Schematic diagram of LMD with some experimental instruments.

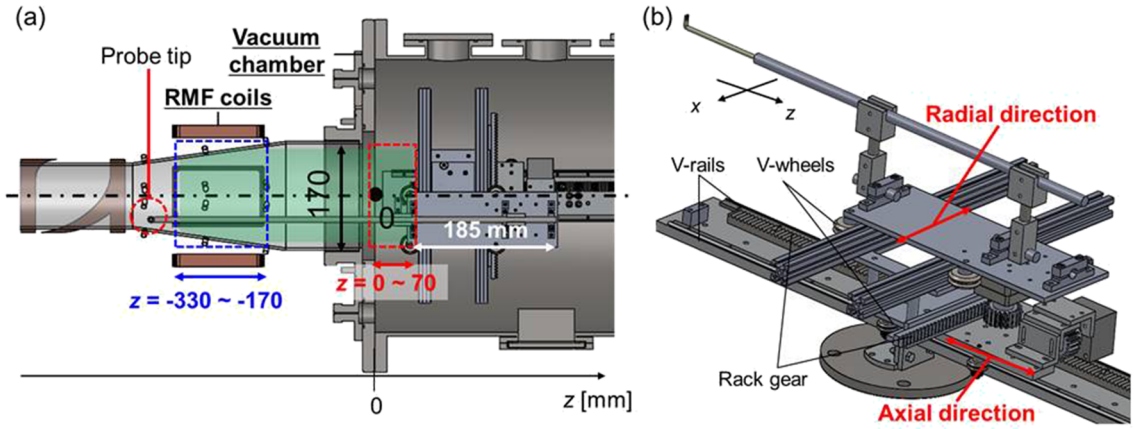


FIG. 2. Schematics of the developed scanning instrument: (a) the measurement 2D area in the green hatched area by the use of the developed instrument and (b) bird eye view of the instrument.

### C. Diagnostics by using scanning instrument and thrust stand

To estimate the electrodeless plasma acceleration effect, $v_i$ and $n_e$ have been measured by using a L-shaped Mach probe, as shown in Fig. 3(a). This probe has two 0.8 mm-diameter and 4 mm-length tungsten rods, which can collect ion saturation currents, separated by using a barrier to deduce the ion Mach number, i.e., ion velocity normalized by an ion sound velocity, considering the unmagnetized model, whose model coefficient is 1.26.[27,28] In addition, we use a typical electron temperature $T_e$ of 3–5 eV, which depends on the measurement position, to derive $v_i$ and $n_e$. Two co-axial cables, covered by using glass sleeves to isolate the outer metal region from a plasma, are connected to the data logger (HIOKI: MEMORY HiCORDER) to display and store probed signals.

With regard to the measurement of time-varying perpendicular component of RMF to the axial axis of $z$ and $\tilde{b}_\perp$, a magnetic probe was used, as shown in Fig. 3(b). This sensor has a two-turn, 10 mm-diameter, co-axial cable with 1.2 mm diameter, considering the signal magnitude, which is in proportion to coil's turn number, signal frequency, surface area, and the strength of the magnetic field. Here, the sensor part is covered by using a ceramic adhesive (Ceramabond 571-Liquid and Powder, Aremco Products, Inc.) to prevent direct-contact between the plasma and the outer metal region. By comparison of $\tilde{b}_\perp$ between w/ and w/o plasma, we can see whether RMF can penetrate fully/partially into plasma or not, using Milroy's expression.[15] The measurement area is under the entire RMF antenna region, whose axial range is from $z = -330$ to $-170$ mm.

We could also mount a target type thrust stand[29] on the axial movable unit, as shown in Fig. 4. The thrust stand has a target board made of polycarbonate, separated two solenoid coils, a laser displacement sensor (KEYENCE: IL-S025), whose resolution is ~1 $\mu$m, and a target hinge to produce the pendulum movement caused by a momentum of plasma flow. As for two separated solenoid coils, one is attached on the stand and can be applied a uniform current, and the other is on the target and can be applied a feedback current, so as to control the axial target movement actively without external force. The electromagnetic force between the two coils by the use of the negative feedback system, attenuates the target displacement $d$. At the stage of calibration to derive a proportionally constant, which determine an equation between thrust force $F$ and $d$ [see Eq. (1)], a known force was applied when pulse current $I$ was applied to both coils, and then the relation between $F$ and $I$ was obtained as shown in Fig. 5(a). Next, relations between target displacement and impulse were obtained in cases of using three pulse durations (50, 100, and 200 ms), considering a deviation by pulse time difference, as shown in

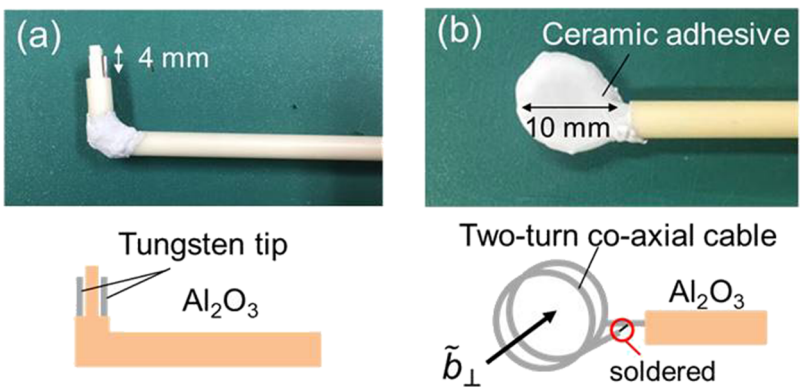


FIG. 3. Schematic views of (a) a L-shaped Mach probe and (b) a magnetic probe to measure $\tilde{b}_\perp$ (red circle indicates a solder part between the outer shield and core wire).

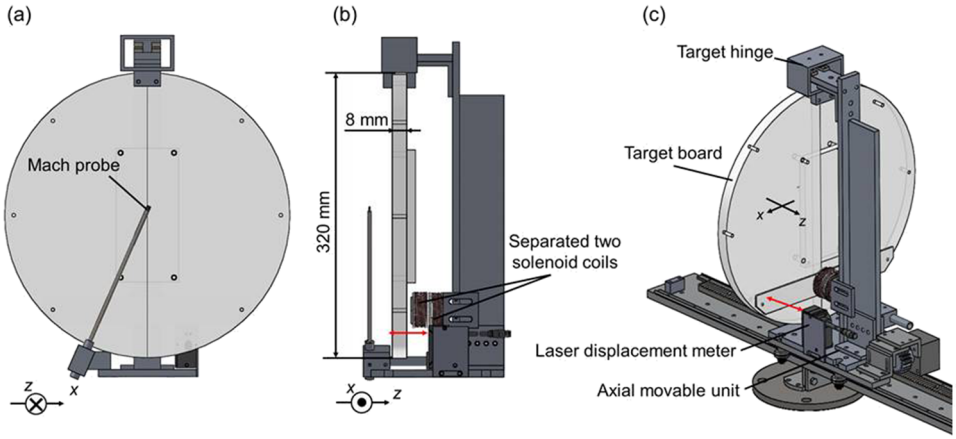


FIG. 4. Schematic views of a developed target type thrust stand on axial movable unit: (a) front, (b) side, and (c) rear left views.

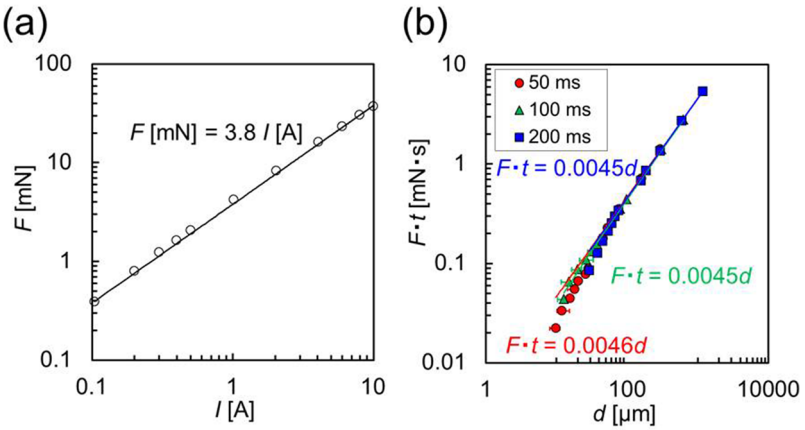


FIG. 5. Calibration results of the target type thrust stand; (a) thrust force $F$ as a function of pulse current value $I$ and (b) impulse $F \cdot t$ as a function of displacement $d$ in pulse durations of 50 (red circles), 100 (green triangles), and 200 ms (blue squares).

Fig. 5(b). Then, the calibration equation was derived as shown in the following equation:

$$F = 4.5 \times 10^{-3}\, d/T. \quad (1)$$

Here, dimensions of $F$, $d$, and $T$, which is impulse time, are (mN), ($\mu$m), and (s), respectively. In our previous experiment, a cylindrical target type[29] was utilized and the present measurement results agreed with those of the previous target type.

Permanent magnets are expected to be practically utilized as an external magnetic field source in the field of plasma propulsion due to no necessity of power supply, since power limitation of space module is a crucial problem for the realization of deep space explorations. Here, some experiments, e.g., helicon/inductively coupled plasma sources with some acceleration methods using permanent magnets have been conducted recently.[30,31]

Now, we will discuss the thrust stand characteristics before showing results, which is described in Sec. III C. Axial profiles of $F$ were measured by using the thrust stand to investigate a thrust performance and plasma diffusion in the radial direction, using the divergent magnetic field, from $z$ of 55 mm to 355 mm at every 50 mm for the case of $P_{rf}$ = 1, 2, and 3 kW, and four kinds of gas flow rate $fr$, as shown in Fig. 6. This can check the effect of the stand positions on the plasma behavior considering the divergent magnetic field configuration in

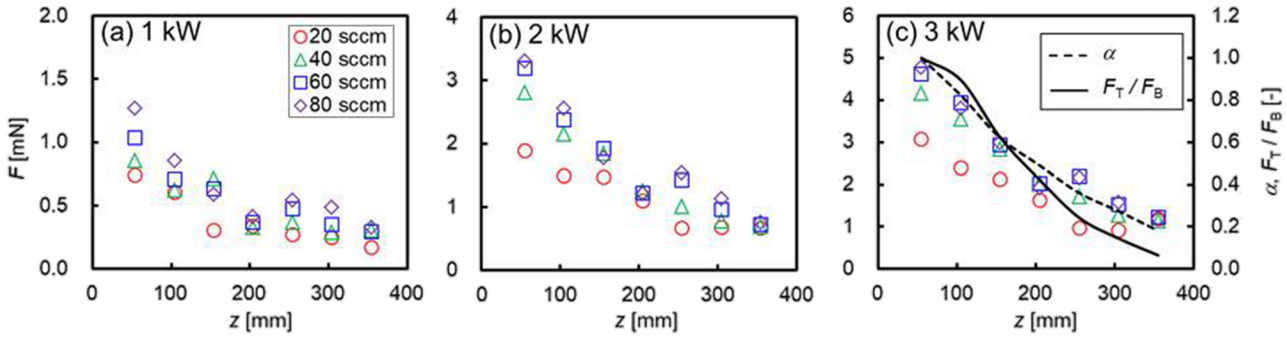


FIG. 6. Axial profiles of $F$ by using the thrust stand in cases of (a) $P_{rf}$ = 1 kW, (b) 2 kW, and (c) 3 kW, and four gas flow rates [20 (red circles), 40 (green triangles), 60 (blue squares), and 80 SCCM (purple diamonds)] using only permanent magnets w/o RMF. In Fig. 6(c), $\alpha$ and $F_T/F_B$ are also described as dotted and bold lines, respectively.

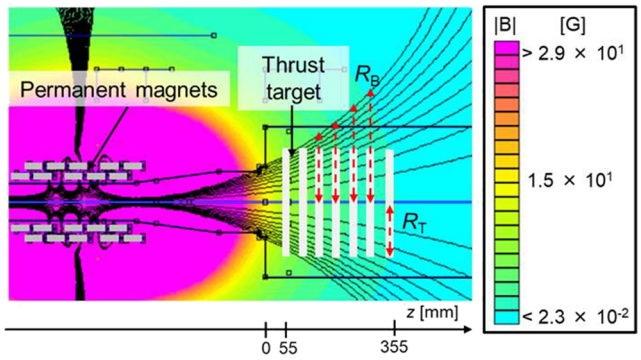


FIG. 7. Magnetic field line of permanent magnet arrays and axial measurement positions of the thrust stand at every 50 mm. In this figure, $R_T$ (constant) and $R_B$ represent the target and the magnetic field spread radii, respectively.

the presence of permanent magnet arrays. Thrust increased by increasing $P_{rf}$ in the entire axial region for all gas flow rate cases (up to ~5 mN for the case of $P_{rf}$ = 3 kW and $fr$ = 80 SCCM at $z$ = 55 mm). With increasing gas flow rate, the thrust values for all experimental conditions seem to be saturated since the increasing rates of $F$, originally caused by an increment of $fr$, decreased. In particular, these $F$ values between $fr$ = 60 and 80 SCCM cases were nearly the same values for all $P_{rf}$ cases. This is considered that a collision between plasma and neutral particles becomes dominant (in typical experimental scheme, Coulomb collision frequency is much lower than neutral collision frequency) by increasing $fr$, leading to the increment of radial electron flux and mobility, although $n_e$ was not measured in this case. The presence of the stand can disturb plasma flow, leading to higher gas pressure in the gas inlet region of LMD. In fact, detected back ground pressure by using an ion gauge (ANELVA: MG-2) attached near the gas inlet port increased from $\sim 3 \times 10^{-4}$ to $\sim 5 \times 10^{-3}$ Pa with mounted thrust stand.

Axial thrust decrement by moving to the downstream region was obtained in Fig. 6, though total thrust should be constant, regardless of the stand position in general and if the plasma does not change with regard to this position. As one of the causes, the ion-neutral collision mentioned above should be considered since neutrals escape from the main plasma without feeling the magnetic field. Here, an ion mean free path of ~6 mm (under a typical case that a neutral pressure is 0.8 Pa with ion temperature $T_i$ = 0.15 eV) can be estimated from the obtained, collisional cross section between an ion and neutral particles from Lieberman's book.[32] Moreover, all plasma particles, including those are along the divergent magnetic field line of permanent magnets, could not be captured by moving the stand to the downstream region due to diffusion and loss, and that might be another cause of the axial thrust decrement, which is discussed next that the plasma performance did not change appreciably with respect to the thrust stand position. Needless to say, ions cannot follow the magnetic field line in the case of the large argon ion Larmor radius $\rho_i$ in the downstream region, where the magnetic field is weak, e.g., $\rho_i \sim 120$ mm in the case of $B$ = 20 G and typical $T_i$ of 0.15 eV.

Here, the ratio of captured plasma thrust to the whole plasma thrust is estimated, considering the divergent magnetic field lines. Figure 7 shows the magnetic field line of permanent magnets and axial measurement positions of thrust stand at every 50 mm. The stand radius $R_T$ has an enough length to capture the field line, whose spread radius is $R_B$, which is a function of $z$ and represents outer most field lines in the presence of the plasma, as shown in Fig. 7. In this estimation, radial ($x$-axis) profiles of $n_e$, regardless of axial position, can be taken as a parabolic function of radius $r$, as shown in the following equation:

$$n_e(r) = n_e(0)\left[1 - \left(\frac{r}{R_B}\right)^2\right]. \quad (2)$$

Here, $n_e(0)$ represents an electron density at $r$ = 0 mm. With respect to the validity of this parabolic assumption, we will explain this in Sec. III A (Fig. 8). In this case, we assume that $v_i$ and $T_e$ are constant in space, and calculate the ratio of surface integral of plasma thrusts $F_T/F_B$. These are expressed as a sum of static pressure $n_e k_B T_e$ ($k_B$: Boltzmann constant) and dynamic pressure $n_e m_i v_i^2$ [the product of ion flux $n_i v_i$ and momentum $m_i v_i$ ($n_i$: ion density and $m_i$: ion mass)] and in our experiment, static pressure was larger than dynamic one from probe measurements, as follows:

$$\frac{F_T}{F_B} = \frac{\int_0^{R_T} \left(n_e k_B T_e + n_e m_i v_i^2\right) 2\pi r dr}{\int_0^{R_B} \left(n_e k_B T_e + n_e m_i v_i^2\right) 2\pi r dr} = \frac{\left(k_B T_e + m_i v_i^2\right) \int_0^{R_T} n_e 2\pi r dr}{\left(k_B T_e + m_i v_i^2\right) \int_0^{R_B} n_e 2\pi r dr} = \frac{\int_0^{R_T} n_e r dr}{\int_0^{R_B} n_e r dr}. \quad (3)$$

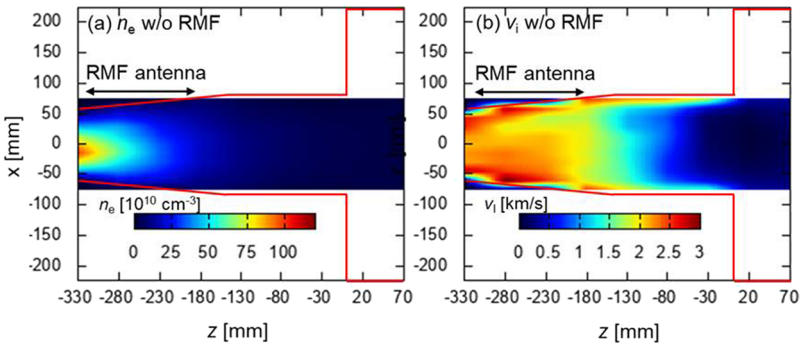


FIG. 8. Two-dimensional profiles of (a) $n_e$ and (b) $v_i$ for the case of $P_{rf}$ = 1 kW and $fr$ = 40 SCCM w/o RMF application.

An approximation formula can be derived from Eqs. (2) and (3) using $\alpha = R_T/R_B$ ($R_T < R_B$) for simplification as follows:

$$\frac{F_T}{F_B} = \alpha^2\left(2-\alpha^2\right)(\alpha \le 1) \text{ and } 1\,(\alpha > 1). \quad (4)$$

By using Eq. (4), we can estimate this thrust ratio in Fig. 6(c) along with the axial profiles of the measured thrust values. The thrust ratio seems to be slightly saturated in $z$ of 55–105 mm. As shown in Fig. 7, the stand surface captures the entire magnetic field lines at $z$ = 55 and 100 mm, which is the nearest measurement position from permanent magnet arrays. Therefore, $F_T/F_B$ seems to saturate at $z$ = of 55–100 mm, as shown in Fig. 6(c), since $F_T/F_B \sim 1$ in the case of $\alpha \ge 1$. In addition, from the curve of $\alpha$ and the ratio of $F_T/F_B$, which roughly agrees with a decay of the thrust, it was confirmed that plasma performance did not change appreciably with respect to the thrust stand position, and appreciable plasma loss across the magnetic field is suggested to be negligible.

In Sec. III, we will compare the RMF thrust performances between using the thrust stand and plasma parameters measured by using a Mach probe, which is attached near the thrust stand with a distance of ~10 mm as shown in left-hand side (LHS) of Fig. 4(b). The stand pre-sheath effect on the Mach probe measurement is negligible, since this distance is much longer than the sheath length near the thrust target surface, several times as of the Debye length, which has a typical value of ~90 $\mu$m (using $n_e = 2.5 \times 10^{10}$ cm$^{-3}$ and $T_e = 4$ eV).

## III. EXPERIMENTAL RESULTS OF RMF ACCELERATION SCHEME

### A. Two-dimensional profiles of $n_e$ and $v_i$

Two-dimensional profiles of $n_e$ and $v_i$ were measured by using the moving system at every $x$ and $z$ of 15 and 50 mm, respectively. Here, Fig. 8(a) shows the spatial profile of $n_e$ w/o RMF, for the case of $P_{rf}$ = 1 kW and $fr$ = 40 SCCM in addition to the axial profiles at $x$ = 0 mm. Figure 9 shows the measured $n_e$ profile (along the $x$ axis) at $z$ = 20 mm in Fig. 8(a) and with a parabolic approximated function curve, where $R_B$ is ~120 mm, derived from the spread line of the divergent magnetic field in Fig. 7. The measured $n_e$ profile agrees well with this approximation curve although the axial position is different from the thrust measurement position. As shown in Fig. 8(a), a decrease of $n_e$ with $z$ from upstream of the RMF antenna region to the downstream is caused by the divergent magnetic field in addition to the ion-neutral collision, as mentioned above.

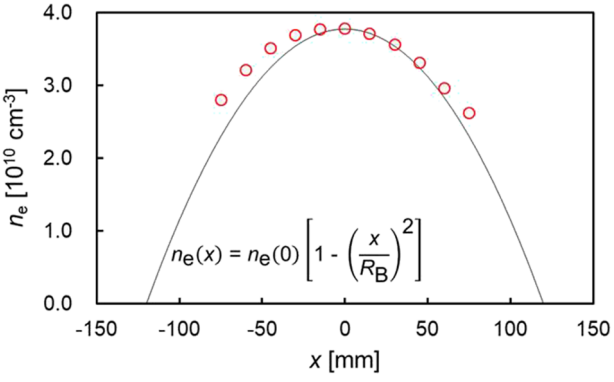


FIG. 9. $n_e$ profile along with the $x$ axis obtained and a parabolic $n_e$ function at $z$ = 20 mm for $P_{rf}$ = 1 kW and $fr$ = 40 SCCM w/o RMF application [from Fig. 8(a)]. Open red circles and real black line mean measured electron density values and the parabolic function, respectively.

With regard to $v_i$, axial decrease of $v_i$ was also found in Fig. 8(b), and one of the reasons is collision between ions and neutral particles in the downstream region. In addition, $v_i$ was higher in the outer radius region than that around $x$ = 0 mm. This may be due to the assumed constant spatial profile of $T_e$, which determines the local ion sound velocity, in deriving the ion Mach number. Namely, there was a tendency experimentally that $T_e$ decreases from the center region toward the edge in the radial direction. Along the downstream region, the increasing rates of $v_i$ increased due to the following reasons: Axial force is expected to be generated by the azimuthal diamagnetic current in the presence of a magnetic nozzle,[33,34] and the axial pressure caused by radial and axial density gradients, respectively, as shown in Fig. 8(a). In order to determine these acceleration mechanisms, dc magnetic field and spatial plasma potential measurements to deduce the electric field should be executed. Here, the axial electric field can be generated for ions to follow the electrons accelerated by these forces. Note that the spatial increasing rates of $n_e$ and $v_i$ have also been obtained with RMF application despite slight differences found.

Here, by using the movable measurement instrument, the spatial characteristics of plasma parameters were obtained, which also enables us to understand acceleration mechanisms in more detail. As next interest, the RMF acceleration effect in using optimal operation conditions should be examined spatially by comparing increasing rates of $n_e$ and $v_i$ between w/o and w/RMF application cases, using this developed scanning instrument.

### B. Two-dimensional profiles of RMF 1D perpendicular component to axial direction by using a magnetic probe

Figures 10(a) and 10(b) show the spatial profiles of RMF 1D perpendicular components to the axial direction, $\tilde{b}_\perp$ in the RMF antennas region by using the magnetic probe, as shown in Fig. 3(b), mounted on the movable instrument with $f_{RMF}$ = 0.7 MHz ($I_{RMF}$ = 55 $A_{pp}$) and 1.5 MHz (20 $A_{pp}$), respectively, w/ and w/o plasma. In Fig. 10(a), the strength of $\tilde{b}_\perp$ w/plasma in the central region of plasma was higher than that of w/o plasma, and RMF penetration into plasma was obtained. However, the central increment might be caused by the existence of wave propagation such as a helicon wave since the S/N ratio was enough to be applied in this frequency range. On the other hand, in the case of $f_{RMF}$ = 1.5 MHz, shown in Fig. 10(b), the RMF current value was lowered to 20 $A_{pp}$ to compare these two different penetration condition cases. The field strength in the center region of plasma decreased so that the penetration into plasma is not enough, which can be understood by Milroy's numerical analysis.[13] The penetration condition of RMF has been investigated experimentally by using the scanning instrument, and in both cases, these magnetic fluxes are conserved due to the increment in the center

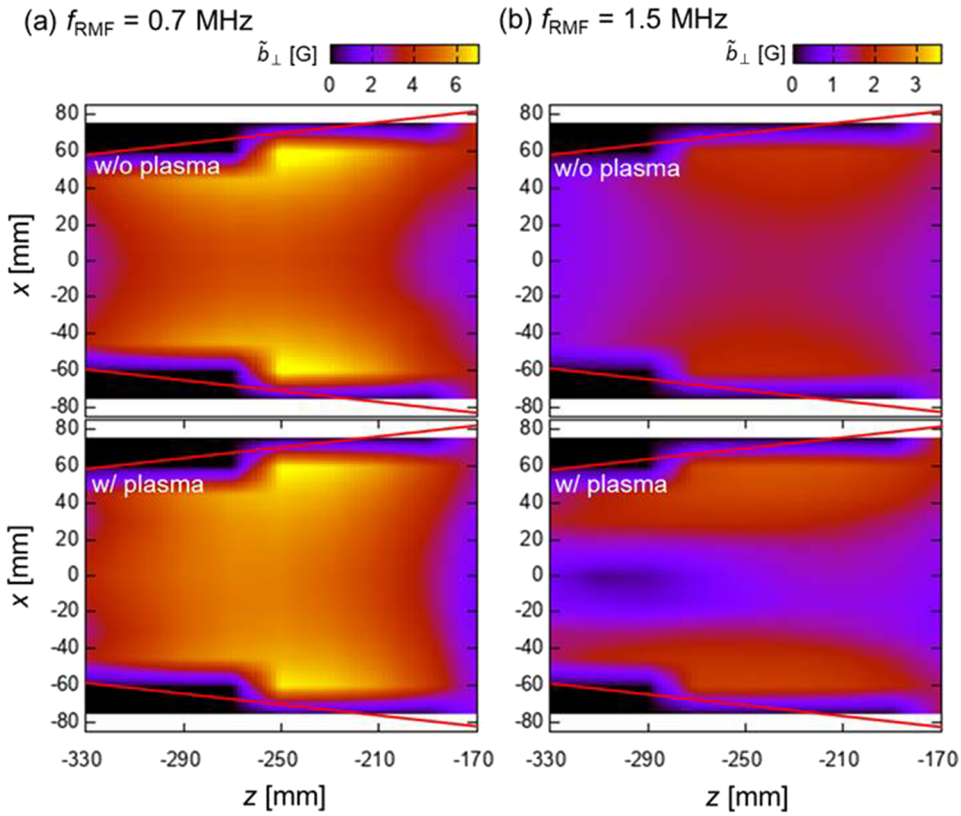


FIG. 10. Two-dimensional profiles of $\tilde{b}_\perp$ components of RMF with (a) $f_{RMF}$ = 0.7 MHz ($I_{RMF}$ = 55 $A_{pp}$) and (b) 1.5 MHz (20 $A_{pp}$) in the RMF antennas region (from $z$ of −330 to −170 mm) w/o and w/plasma.

region and the decrement in the outer region in the same cross section. In order to estimate the electromagnetic acceleration by the RMF method, we need to derive induced $j_\theta$ by measuring three-directional ($x$, $y$, $z$) $2f_{RMF}$ components due to nonlinear terms,[12] using the formula of $\nabla \times \mathbf{B} = \mu_0 \mathbf{j}$ for future studies.

### C. Thrust performance measured by using a target type thrust stand

Figures 11(a) and 11(b) show that thrust performance was measured by using the target type thrust stand located at $z$ = 55 mm, as well as by using a Mach probe. Dependences of thrust $F$ measured by the thrust stand on RMF current $I_{RMF}$, using three flow rates in the case of $P_{rf}$ = 1 kW, are described in Fig. 11(a). Here, $F$ increased by increasing $I_{RMF}$ for all flow rate cases, and the maximum value was obtained, up to ~7 mN using 60 SCCM. The result was not so much different between $fr$ = 40 and 60 SCCM cases. It can be considered that a collision effect between ions and neutral particles could be large as described in Sec. II C. We should survey the $fr$ value to derive the optimal RMF acceleration conditions for future studies.

Figure 11(b) shows the plasma thrust value, which was derived from probe measurement, mounted on the scanning instrument as shown in Fig. 4, and also the thrust value measured by the thrust stand, in the case of $P_{rf}$ = 3 kW, $fr$ = 60 SCCM, and $I_{RMF}$ = 55 $A_{pp}$. The plasma thrust came from the sum of static and dynamic pressures, which are described as surface integrals of $n_e k_B T_e$ and $n_e m_i v_i^2$, respectively, as was mentioned. Here, profiles of $n_e$ and $v_i$ along with the $x$ axis were taken as half values at $r$ = 0 mm and $z$ ~ 40 mm deducing these parabolic profiles. The direct-measured thrust values by the thrust stand are nearly consistent with those derived from probe measurements so that the validity of the thrust measurement was confirmed.

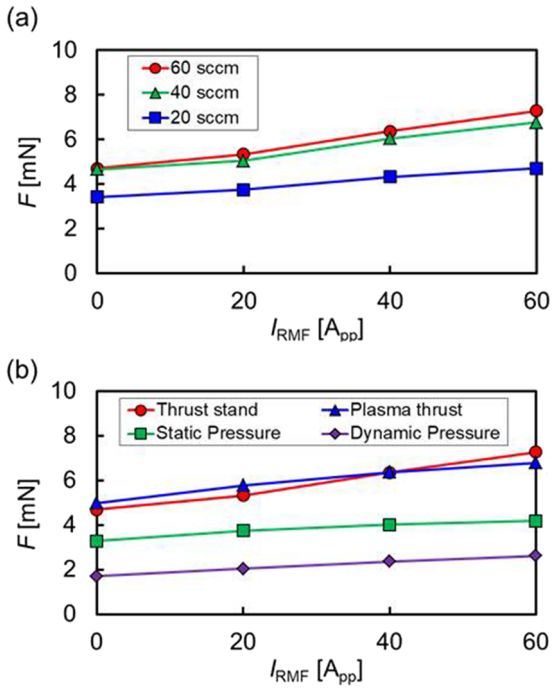


FIG. 11. (a) Measured $F$ by changing $I_{RMF}$ for three flow rate cases (20, 40, and 60 SCCM are expressed as blue squares, green triangles, and red circles, respectively) and (b) comparison between directly measured thrust and calculation values of plasma thrust, i.e., sum of static and dynamic pressures, respectively, using 60 SCCM, in the case of $P_{rf}$ = 3 kW with $f_{RMF}$ = 0.7 MHz (measured thrust, plasma thrust, static pressure, and dynamic pressure are expressed as red circles, green squares, blue triangles, and purple diamonds, respectively).

## IV. CONCLUSION

A two-dimensional scanning instrument has been developed to measure spatial profiles in our RMF acceleration scheme from the RMF antenna region to the inner vacuum chamber region, as shown in Fig. 1. Herewith, spatial profiles of plasma parameters, including $n_e$, $v_i$, and $\tilde{b}_\perp$, w/ and w/o plasma, were obtained. In terms of $n_e$, the decrement in the axial direction was found, which might be caused by a radial loss of plasma by the divergent radial magnetic field and a collision with neutral particles. In addition to permanent magnets, in future, application of electromagnets[35] is expected to be applied to converge the external magnetic field shape for the purpose of decreasing the radial loss and enhancement of plasma axial exhaust. A higher value of $v_i$ in the outer radial region was found regardless of w/ and w/o RMF though $v_i$ increased by applying the RMF method. Furthermore, the azimuthal diamagnetic current leading to the axial Lorentz force and electric field caused by a balance between electron and ion flows should also be considered in the presence of the divergent magnetic field. Detailed spatial electron temperature survey will be required by using electrostatic probes since the profile of $T_e$, which is used to calculate the ion Mach number, is related to the $v_i$ profiles.

As well as movable probing instruments, a new developed, target type thrust stand with the calibration results were described in this paper. Especially, the axial profiles of thrust w/o RMF are meaningful to examine an influence of the target size and axial measurement position on plasma thrust. In our present experiment, the thrust stand was reliable to capture the entire plasma flow along the divergent magnetic field. Of course, if the stand is further away from the source region, it cannot capture the whole plasma in this magnetic field configuration, as shown in Fig. 7. For a future study, a smaller target type thrust stand to scan radial profiles, is expected to be developed. Two-dimensional experimental results of rf RMF components using a magnetic probe were also shown in this paper, and full/partially RMF penetrations into plasma were demonstrated by comparison of the field strength between w/ and w/o RMF application.

Plasma thrust w/RMF was measured, changing $I_{RMF}$ from 0 to 60 $A_{pp}$ with $f_{RMF}$ = 0.7 MHz for the case of $P_{rf}$ = 3 kW, by using the thrust stand, and the thrust value was consistent with that from probe measurements of $n_e$ and $v_i$, and the thrust value increased up to 7 mN by applying RMF in that experimental conditions. In order to derive these acceleration effects, the azimuthal current derived from the RMF scheme is expected to be examined by measuring $2f_{RMF}$ components of RMF induced by a nonlinear effect, as mentioned above (calculation of the induced azimuthal current of this frequency is comparable to the dc induced component). Thus, we are going to introduce the $2f_{RMF}$ component of induced azimuthal current by using a magnetic probe mounted on the developed, scanning instrument, as mentioned in Sec. III B and derive the axial Lorentz force in future.

## ACKNOWLEDGMENTS

We appreciate the prior research of RMF acceleration scheme by Messrs. H. Ishii and S. Otsuka in our group and useful discussions made by HEAT project members. This study has been partially supported by Grand-in-Aid for Scientific Research (Nos. S: 21226019 and B:17H02995) from the Japan Society for the Promotion of Science.

[1] I. H. Hutchinson, Plasma Phys. Controlled Fusion **44**, 2603 (2002).
[2] W. E. Amatucci, J. Geophys. Res.: Space Phys. **104**, 14481, https://doi.org/10.1029/1998ja900098 (1999).
[3] I. Langmuir and H. M. Mott-Smith, Gen. Elec. Rev. **27**, 449 (1924).
[4] I. H. Hutchinson, Phys. Rev. A **37**, 4358 (1988).
[5] K.-S. Chung and I. H. Hutchinson, Phys. Fluids B **1**, 2229 (1989).
[6] T. Dote, Jpn. J. Appl. Phys., Part 1 **7**, 964 (1968).
[7] X. Pei Lu and M. Laroussi, Appl. Phys. Lett. **92**, 051501 (2008).
[8] E. A. Den Hartog, H. Persing, and R. Claude Woods, Appl. Phys. Lett. **57**, 661 (1990).
[9] D. Kuwahara, Y. Tanida, M. Watanabe, N. Teshigahara, Y. Yamagata, and S. Shinohara, Plasma Fusion Res. **10**, 3401057 (2015).
[10] Y. Tanida, D. Kuwahara, and S. Shinohara, Trans. Jpn. Soc. Aeronaut. Space Sci., Aerosp. Technol. Jpn. **14**, Pb_7 (2016).
[11] K. Muraoka and A. Kono, J. Phys. D: Appl. Phys. **44**, 043001 (2011) (review paper).
[12] S. Shinohara, H. Nishida, T. Tanikawa, T. Hada, I. Funaki, and K. P. Shamrai, IEEE Trans. Plasma Sci. **42**, 1245 (2015).
[13] S. Shinohara, J. Plasma Fusion Res. **91**, 412 (2015) (project review paper) [in Japanese].
[14] I. R. Jones, Phys. Plasmas **6**, 1950 (1999).
[15] R. D. Milroy, Phys. Plasmas **6**, 2771 (1999).
[16] S. Otsuka, K. Takizawa, Y. Tanida, D. Kuwahara, and S. Shinohara, Plasma Fusion Res. **10**, 3401026 (2015).
[17] T. Furukawa, K. Takizawa, D. Kuwahara, and S. Shinohara, Phys. Plasmas **24**, 043505 (2017).
[18] T. Furukawa, K. Takizawa, D. Kuwahara, and S. Shinohara, AIP Adv. **7**, 115204 (2017).
[19] S. Shinohara, Adv. Phys.: X **3**, 1 (2018).
[20] R. W. Boswell, Phys. Lett. A **33**, 457 (1970).
[21] D. M. Goebel, IEEE Trans. Plasma Sci. **36**, 2111 (2008).
[22] V. V. Zhurin, H. R. Kaufman, and R. S. Robinson, Plasma Sources Sci. Technol. **8**, R1 (1999).
[23] M. Martinez-Sanchez and J. E. Pollard, J. Propul. Power **14**, 5 (1998).
[24] S. Otsuka, T. Nakagawa, H. Ishii, N. Teshigahara, H. Fujitsuka, S. Waseda, T. Ishii, D. Kuwahara, and S. Shinohara, Plasma Fusion Res. **9**, 3406047 (2014).
[25] S. Shinohara, S. Takechi, and Y. Kawai, Jpn. J. Appl. Phys., Part 1 **35**, 4503 (1996).
[26] F. F. Chen, Plasma Phys. Controlled Fusion **33**, 339 (1991).
[27] M. Hudis and L. M. Lidsky, J. Appl. Phys. **41**, 5011 (1970).
[28] K. S. Chung, I. H. Hutchinson, B. Labombard, and R. W. Conn, Phys. Fluids B **1**, 2229 (1989).
[29] D. Kuwahara, Y. Koyama, S. Otsuka, T. Ishii, H. Ishii, H. Fujitsuka, S. Waseda, and S. Shinohara, Plasma Fusion Res. **9**, 3406025 (2014).
[30] F. F. Chen, Phys. Plasmas **19**, 093509 (2012).
[31] K. Takahashi, K. Oguni, and A. Ando, Phys. Plasmas **15**, 084501 (2008).
[32] M. A. Lieberman and A. J. Lichtenberg, *Principles of Plasma Discharges and Materials Processing* (John Wiley & Sons, Inc., New York, 1994).
[33] K. Takahashi, T. Lafleur, C. Charles, P. Alexander, and R. W. Boswell, Phys. Rev. Lett. **107**, 235001 (2011).
[34] A. Fruchtman, K. Takahashi, C. Charles, and R. W. Boswell, Phys. Plasmas **19**, 0033507 (2012).
[35] D. Kuwahara, S. Shinohara, and K. Yano, J. Propul. Power **33**, 420 (2017).